Enhanced Chemical and Electrochemical Water Oxidation Catalytic Activity by Hybrid Carbon Nanotube-based Iridium Catalysts Having Sulfonate-functionalized NHC ligands

Jorge Nieto,[a] M. Victoria Jiménez,[a] Patricia Álvarez,[b*] Ana M. Pérez-Mas,[b] Zoraida González,[b] Rafael Pereira,[a] Beatriz Sánchez-Page,[a] Jesús J. Pérez-Torrente[a] Javier Blasco,[c] Gloria Subias,[c] Matias Blanco,[b]† and Rosa Menéndez.[b]*

[a]Departamento de Química Inorgánica, Instituto de Síntesis Química y Catálisis Homogénea-ISQCH, Universidad de Zaragoza-C.S.I.C., 50009-Zaragoza, Spain.

[b]Instituto Nacional del Carbón-INCAR, C.S.I.C., 33011-Oviedo, Spain.

[c]Instituto de Ciencia de Materiales de Aragón-ICMA, Departamento de Física de la Materia Condensada, CSIC-Universidad de Zaragoza, 50009 Zaragoza, Spain.

* Corresponding authors' email: vjimenez@unizar.es, par@incar.csic.es

ABSTRACT

The hybrid materials resulting from the covalent attachment of iridium NHC complexes bearing 3-methyl-imidazol-2-ylidene and 3-(propyl-3-sulfonate)-imidazol-2-ylidene ligands to carbon nanotubes through ester functions, efficiently catalyzed water oxidation under chemical and electrochemical conditions. The hybrid catalyst featuring an NHC ligand with a propyl-sulfonate wingtip has shown an improved catalytic performance compared to that of the unfunctionalized material with TOF_{50} numbers up to 1140 h^{-1} using ammonium cerium(IV) nitrate (CAN) as electron acceptor at [CAN]/[Ir] ratios higher than 2000. The positive effect of the presence of a polar sulfonate group in water oxidation has been also observed in related molecular catalysts with compound $[Ir(cod)\{MeIm(CH_2)_3SO_3\}]$ being more active than $[IrCl(cod)\{MeIm(CH_2)_3OH\}]$. The hybrid catalysts were less active than the molecular catalysts although their productivity has been improved by allowing successive additions of CAN or at least three recycling experiments. The electrochemical water oxidation by CNT-based hybrid materials resulted much more efficient. The positive influence of a water soluble sulfonate wingtip in the hybrid catalysts has been also identified allowing with TOF values close to 22000 h^{-1} at 1.4 V. The local structure around iridium atoms in the heterogeneous catalysts has been determined by means of EXAFS applied before and after water oxidation reactions. The first coordination shell is similar in both fresh and post-catalytic catalysts but a slightly increase in the oxidation state of iridium atoms is observed what can be correlated to the peaks shifts in the XPS spectra for the oxidized materials.

Keywords: water oxidation, carbon nanotubes supports, iridium, N-heterocyclic carbenes (NHC), water soluble ligands

INTRODUCTION

Water splitting and CO_2 reduction are key reactions able to produce such important chemical fuels as hydrogen, oxygen and hydrocarbons, respectively. In both processes, the bottle neck relies on the catalytic water oxidation (WO). In fact, the complex process of removing four electrons and four protons from two water molecules with concomitant formation of an O=O double bond ($2H_2O \rightarrow O_2 + 4H^+ + 4e^-$) has made catalytic WO a major challenge for the later decades.[1,2] Mimicking the nature to develop efficient and robust photocatalyst materials that absorb the solar photons to convert solar energy into chemical energy is a major goal nowadays.[3]

In addition to heterogeneous photocatalyst materials (metal oxides, (oxy)sulfides, (oxy)nitrides or metal (oxy)nanoparticles), a large number of transition metal homogeneous systems based mainly on Ru, Ir, Fe, Mn complexes, polyoxometalates or metallo-organic frameworks (MOFs) integrated into electrochemical and photoelectrochemical cells, have attracted considerable attention[4,5,6] because of their rapid and high oxygen evolution efficiency and their more tunable structures comparing to those of the heterogeneous systems. Although earth-abundant first-row transition metals have been recently described as efficient water-oxidation catalysts because of their low cost, low toxicity and high natural abundance of these metals,[7] remarkably most of the molecular water oxidation catalysts developed to date are based on ruthenium and iridium transition metals.[8,9]

The employment of N-heterocyclic carbene (NHC) ligands in transition metal complexes has generated much more active catalysts[10] than the first iridium known catalyst [Ir(ppy)$_2$(OH$_2$)$_2$]OTf containing cyclometalated 2-phenylpyridine (ppy) ligands reported by Bernhard.[11] Thus, a series of efficient iridium water oxidation catalysts featuring powerful electron donating NHC ligands with improved catalytic activity have been recently

reported,[12] but much remains to be explored, especially dealing with the stability.[13,14] The assessment of WOCs can be carried out under chemical, electrochemical and photochemical driven conditions.[15] Although, the chemical water oxidation driven by sacrificial oxidants, such as Ce^{4+}, IO_4^-, or $S_2O_8^{2-}$, has the advantage that it allows a rapid screening and tuning of the catalysts, it also has serious limitations dealing with the catalyst stability in the presence of strong chemical oxidants, sometimes working under very acidic conditions what provokes the oxidative degradation of the ancillary ligands. On the other hand, the electrochemical approach allows working in milder conditions of pH without sacrificial oxidants, even though the stability of the material under working conditions becomes critical.[16]

In view of their activity and future application as devices for water splitting, it is essential to immobilize homogeneous catalysts, particularly via covalent attachment, on surfaces of heterogeneous electrodes what could offer also additional advantages as reducing the amount of catalyst needed with enhancing efficiency and robustness or as preventing deactivation via associative intermolecular pathways when grafted.[12,17,18] Several homogeneous and heterogeneous WOCs have been immobilized onto electrodes for electrochemical water oxidation, either by anchoring molecular WOCs to oxide electrodes through carboxylate or phosphonate functionalities[19,20] or by deposition of nanoparticle or polyoxometalate WOCs onto electrodes.[21,22] Although, MOFs have demonstrated its efficiency as suitable transition metal support,[12] the insulating nature of most of them difficult their application in electrocatalytic systems. Alternatively, carbon-based materials are one of the most versatile matrixes for developing WOC heterogeneous catalysts.[23,24,25] Multiwalled carbon nanotubes (CNTs), as a particular class within this type of carbon nanostructures, are extraordinary thermal and hydrothermal stable materials,[26] with high area and surface adsorption which facilitates molecule activation[27] along with an interesting confinement effect.[28]

We have recently reported the covalent linkage of Ir[I]-NHC complexes to functionalized CNTs via ester or acetyl linkers to prepare robust active catalysts in hydrogen transfer reactions.[29,30] This strategy required an initial mild oxidation of the CNTs previous to the functionalization which also increases the polarity of their surfaces. This is of particular importance for reactions in water as WOC. However, this polarity increase is rather limited as part of the polar groups will be used to covalently attach the Ir-NHC complex. Bearing that in mind and knowing the rather limited number of heterogenized iridium WOCs reported so far in the literature,[12] our approach for the design of efficient water oxidation catalysts is the synthesis of a new hybrid CNT-based Ir[I]-NHC catalyst containing a water-soluble NHC ligand. The aim of this study is to investigate the effect that the increment in polarity with respect to the original materials lacking water soluble ligands has in their suitability as WOCs. The WOC efficiency for these hybrid catalysts has been evaluated using two strategies: i) via chemical oxidation using Ce^{4+} as sacrificial oxidant and, in consequence, under strong acidic conditions, and ii) via electrochemical oxidation once the electrodes were conformed. To the best of our knowledge, this report constitutes the first examples of carbon nanotube supported Ir[I]-NHC complexes as water oxidation catalysts.

RESULTS AND DISCUSSION

Synthesis and Characterization of CNT-based Iridium–NHC Hybrid Catalysts.

The imidazolium salts [MeImH(CH$_2$)$_3$OH]Cl (**1**) and [HO(CH$_2$)$_2$ImH(CH$_2$)$_3$SO$_3$] (**2**) were anchored on the CNTs through their -OH functions by reaction with the acid groups of oxidized CNTs,[31] located at the edges of the walls, previously treated with thionyl chloride following the procedure described by us and detailed in the Experimental Section.[30] Operating in such a way, it was possible to obtain the functionalized carbon nanotube

materials named **CNT-1** and **CNT-2**, featuring 3-methyl-1*H*-imidazolium and 3-(propyl-3-sulfonate)-1*H*-imidazolium fragments, respectively, linked to the CNT through ester functions. The anchoring of the hydroxy-functionalized imidazolium salt to the carbon nanotube was confirmed by ^{1}H$_{PRESAT}$ NMR[32] of water suspensions of the materials that showed two resonances in the range δ 7.48–7.59 ppm (H4 and H5) and a resonance at δ 8.72–8.88 ppm (H2) typical of imidazolium rings. Noteworthy, the highest solubility of **CNT-2** in water, due to the presence of the sulfonate wingtip at the imidazolium fragment, resulted in improved NMR resolution.
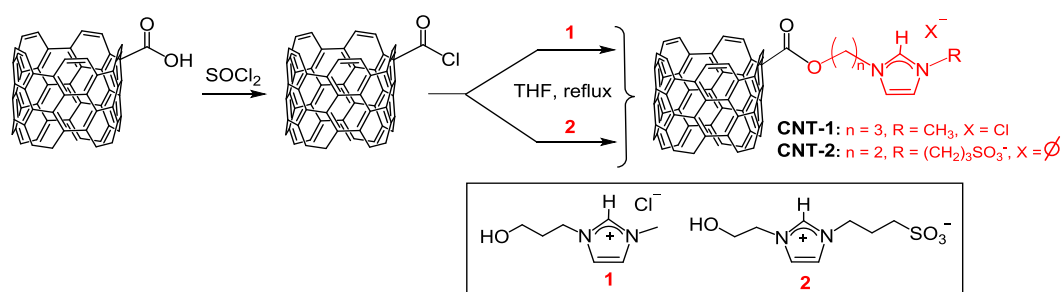
Scheme 1. General procedure for the covalent functionalization of oxidized carbon nanotube materials with hydroxyl-functionalized imidazolium salts via ester linkers.

The imidazolium-functionalized CNT materials were analyzed by means of XPS and elemental analysis (Table S1, Supporting Information). The successful functionalization of the nanotubes was confirmed by the increment in the atomic percentage of nitrogen from 0.4% in the parent material to 1.5 and 2.6%, for **CNT-1** and **CNT-2**, respectively. Additionally, **CNT-2** exhibits a 1.6 % of sulfur, not detected in the parent material, which is associated to the presence of sulfonate groups. The increase in the atomic C/O ratio from ~3 in the starting CNTs to ~6/7 in the functionalized materials can be also attributed to the covalent linkage of the functionalized-imidazolium salts to the nanotube. In accordance with this, a steady increase in the amount of nitrogen was observed in the elemental analyses which also support the functionalization of the CNT materials. In contrast to **CNT-1**, the

differences between the atomic and elemental nitrogen percentage in **CNT-2** (calculated by means of XPS and elemental analysis respectively) suggest that the functionalization on the external surface of the tubes is higher than in the inner cavity which could be a consequence of the more hydrophilic of **CNT-2** due to the presence of the propyl-sulfonate wingtip.

The analysis of the functional groups by high resolution XPS C1s band of their spectra show a decrease of carboxylic acid together an increase of its ester COOR moieties comparing with the oxidized starting material (Table S1, Supporting Information). This could be probably associated to the transformation of the acids into ester functions due to linkage with the hydroxyl-functionalized imidazolium salts, but these materials still have a large percentage of oxygen as a consequence of remaining unreactive hydroxyl, epoxy or ether groups.[33] Additionally, there is an increase of the C-X band at 285.5 eV, which could also be attributed to the C-N moieties of the imidazolium ring overlapping the C-O of parent CNT after functionalization. This increment is substantially larger in **CNT-2** due to the presence of the C-S bonds of the propyl-sulfonate wingtip, also overlapping this C-X band.[34]

The quantification of bonded imidazolium salt to the carbon nanotube was estimated by means of thermogravimetric analysis (TGA, Supporting Information). The weight losses at 400 ºC, 16 wt.% for **CNT-1** and 18 wt.% for **CNT-2**, correspond to the whole imidazolium fragment,[35] should be related with the elemental analysis of the materials and give comparative estimation of the molar percentages in nitrogen/carbon in both materials by taking into account the molecular weight of the imidazolium fragment.[36]

The hybrid materials bearing "Ir(cod)" metal fragments coordinated to imidazol-2-ylidene ligands anchored to the carbon nanotubes through ester functions, **CNT-1-Ir** and **CNT-2-Ir**, were prepared by deprotonation of the weak acid proton at the C2 of the supported imidazolium groups by the basic methoxo ligands in the dinuclear complex [Ir(μ-

OMe)(cod)]$_2$ (cod = 1,5-cyclooctadiene) (Scheme 2). Methanol was detected by gas chromatography what points to the progress of the reaction. However, these materials are quite insoluble due to the increment in the molecular weight of functionalized carbon nanomaterials produced after the metal coordination which avoids their characterization by conventional NMR techniques.
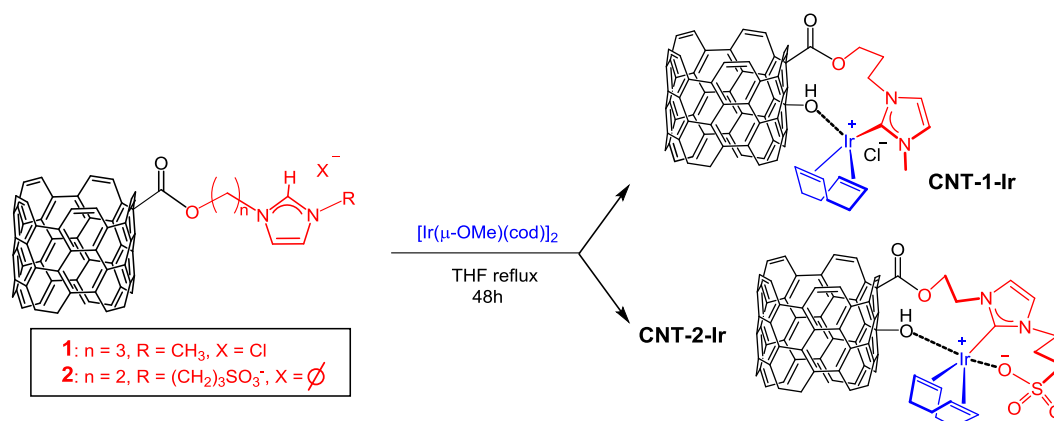
Scheme 2. General procedure for the synthesis of hybrid carbon nanotube-based Ir^{I}-NHC catalysts.

It was no possible to characterize these Ir-NHC hybrid materials by solid-state ^{13}C-CPMAS NMR spectra because of their very broad resonances produced by the high number of walls in the materials together their own heterogeneity.[37] Anyhow, the coordination sphere for the iridium complexes is supposed to be formed at least by the diolefine and the NHC ligand, and it should be completed by the chlorido ligand in **CNT-1-Ir** or the anionic sulfonate fragment in **CNT-2-Ir**, or alternatively any coordinating group on the CNTs wall for both. As a matter of fact, EXAFS analysis has been performed over the known **CNT-1-Ir** and the study concludes that the fourth coordination position is occupied by a light element what could be in accordance with an oxygen from the wall, but not with a chlorido ligand coming from the imidazolium salt.[38] Thus, a similar coordination can be proposed for iridium centers in the hybrid material **CNT-2-Ir**, with the coordination sphere completed by an oxygen from the

8

nanotube material, although coordination of an oxygen from the sulfonate group cannot be ruled out due to its coordinative capacity.

The HRTEM images of **CNT-1-Ir** and **CNT-2-Ir** (Figure 1a and 1b, respectively) confirm the presence of homogeneous distributions of electrondense regions with diameters ranging 0.15–0.30 nm all throughout the outer and inner walls (white circles). The metallic spots are in the range of the molecular iridium complexes as confirmed by their EDX spectra (see Supporting Information). Larger iridium particles of 1.2–1.4 nm also detected, mainly in outer walls, could be the case of clusters[39] or nanoparticles[40] possibly formed during beam irradiation inside the microscope chamber.[41] Similar size distributions were observed for other supported molecular iridium catalysts[29,30,42] or even for graphene-based Ir-NHC hybrid catalysts.[43] In spite of those larger spots, the Ir-4f core level XPS spectra of both samples (Figure 1c) show two maxima of binding energies centered at 62.4 and 65.3 eV, corresponding to Ir-4f$_{7/2}$ and Ir-4f$_{5/2}$. Similar values were measured for related Ir^{I} species anchored to nanotube or graphene materials.[29,30,43,44,45]
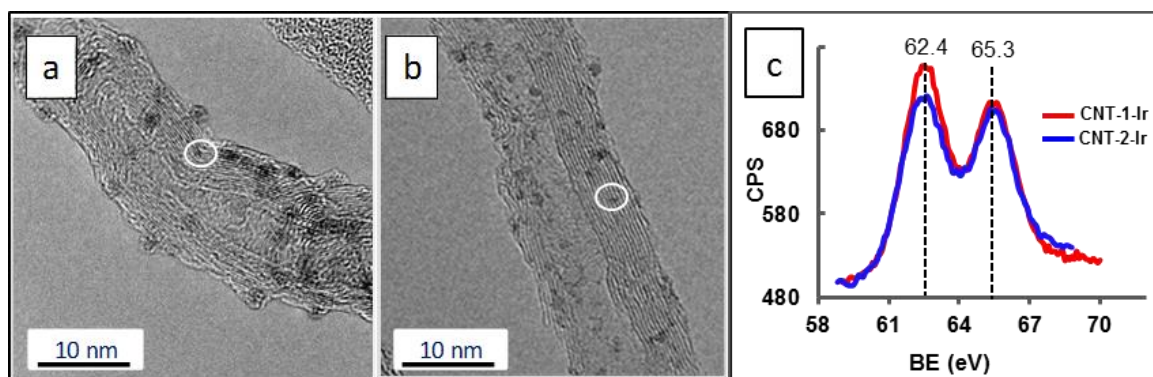

Figure 1. HRTEM images of the carbon nanotube-based Ir^{I}-NHC hybrid catalysts **CNT-1-Ir** (a) and **CNT-2-Ir** (b). XPS Ir4f spectra of **CNT-1-Ir** and **CNT-2-Ir** (c).

The amount of iridium in the hybrid catalysts determined by means of ICP-MS was 10.1 wt.% for **CNT-1-Ir** and 8.8 wt.% for **CNT-2-Ir**. Based on the nitrogen introduced into each

nanotube sample (two nitrogen atoms per imidazol-2-ylidene ring), the maximum amount of iridium that can be loaded can be calculated and allows estimating an almost quantitative functionalization for **CNT-1-Ir** and *ca.* 90% for **CNT-2-Ir**.

In order to gain an insight into the local structure of the iridium atoms in the hybrid catalysts, X-ray absorption spectroscopy (XAS) measurements were performed at room temperature. Figure 2a presents the k^2-weighted EXAFS signals for the new **CNT-2-Ir** compared to the known **CNT-1-Ir** hybrid catalyst and [IrCl(cod){MeIm(CH$_2$)$_3$OH}] as reference compound whose structures have been already determined.[38] The EXAFS signal of the reference compound shows a characteristic interference at k ~8-10 Å^{-1} ascribed to the contribution of the Ir-Cl path. This interference is lacked for the hybrid materials indicating that the first coordination shell around Ir atoms is only composed by light elements. As has been said, our previous study of EXAFS of **CNT-1-Ir** determined that Cl atom is replaced by an oxygen atom from oxidized groups of CNT wall and the Ir atom is surrounded by 5 C, 4 olefin carbons and 1 from the imidazol-2-ylidene ligand, and 1 O. In the case of **CNT-2-Ir**, the expected first coordination shell is also composed of 5 C (4 of them from the diolefine and the fifth from the imidazol-2-ylidene ligand) and 1 O, either from the sulfonate group or from the CNT wall (Scheme 2). However, **CNT-2-Ir** and **CNT-1-Ir** catalysts exhibit alike oscillations indicating similar environment for Ir atoms beyond the first coordination shell (Figure 2a).
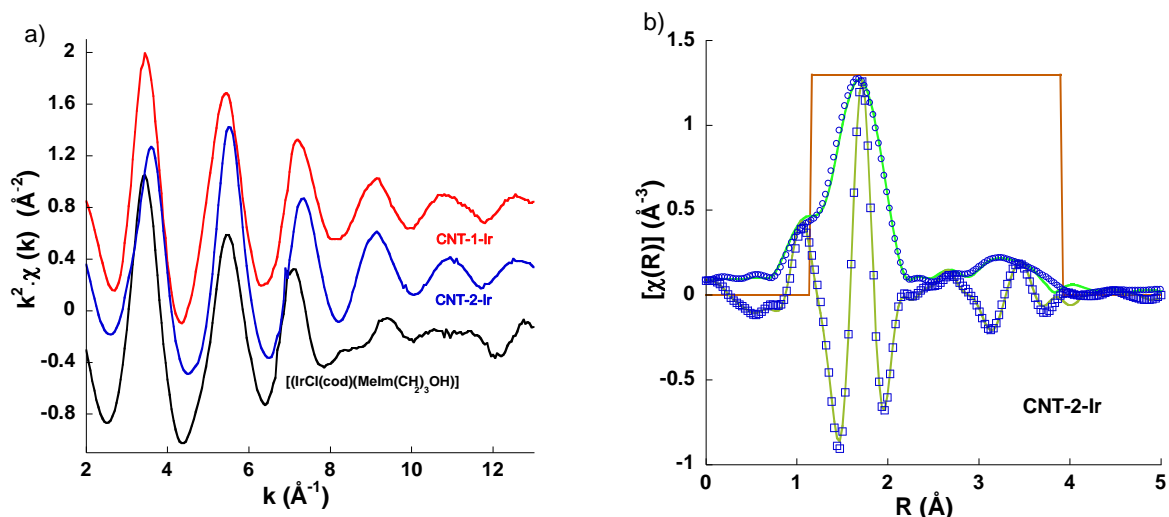
Figure 2. (a) k^2-weighted EXAFS spectra for the fresh hybrid catalysts **CNT-1-Ir**, **CNT-2-Ir** and the reference [IrCl(cod){MeIm(CH$_2$)$_3$OH}] compound. The data are shifted in the vertical scale to compare. (b) Fits (green lines) and experimental (points) Fourier transform curves (circles for modulus and squares for the real part) of the k^2-weighted EXAFS signal of the fresh hybrid catalyst **CNT-2-Ir**. The Hanning window used to filter the signal is also included.

As there is not crystallographic information available for a related alkyl-sulfonate-iridium(I) complex, we have followed our previous strategy in order to model the Ir environment. We have taken the crystal data from X-ray diffraction study of a single crystal of compound [IrCl(cod){MeIm(CH$_2$)$_3$OH}][43] and replaced the Cl atom by an oxygen atom located at ~2.03 Å from the Ir atom. Thus, phases and amplitudes of the different paths were calculated using the FEFF6.0 code implemented in the Artemis program.[46] This model allows us to fit the first and second coordination shells. The analysis is limited by the quality of the EXAS spectra, so the useful ranges were limited to Δk ~2.0-12.5 Å^{-1} and ΔR~1.1-3.9 Å. In order to elucidate the possible coordination of the O-SO$_2$- groups to the metal center, phases and amplitudes for Ir-O-S paths (single and multiple scattering) were calculated from the X-ray diffraction crystal data of the fluorosulfate iridium(III) compound, *mer*-[Ir(CO)$_3$(OSO$_2$F)$_3$].[47] The

11

addition of these paths does not allow accurate fits for the **CNT-2-Ir** spectra thereby suggesting that sulfonate group is not present in the Ir environment in the hybrid catalysts and that this position is occupied by oxygen groups on the nanomaterial wall as it was previously observed for **CNT-1-Ir**. Accurate fits (Figure 2b) can be obtained by considering only contributions from cod and a imidazol-2-ylidene ring as happens for **CNT-1-Ir**. The full analysis, including second shell, can be found in the Supporting Information. The first shell of the two hybrid catalysts can be accounted for by 6 light elements (namely 5 C and 1 O) with bond lengths ranging between 1.99 and 2.2 Å.

Synthesis and Characterization of Iridium(I) Complexes with Related Functionalized-NHC Ligands.

With the aim to compare the activity/structure of the hybrid catalysts **CNT-1-Ir** and **CNT-2-Ir** with analogous homogeneous catalysts, the molecular compounds containing NHC ligands derived from hydroxy- or sulfonate-functionalized imidazolium salts [MeImH(CH$_2$)$_3$OH]Cl (**1**)[48] and [MeImH(CH$_2$)$_3$SO$_3$] (**3**)[49] were synthesized. Complexes [IrCl(cod){MeIm(CH$_2$)$_3$OH}] (**1-Ir**) and [Ir(cod)(MeIm(CH$_2$)$_3$SO$_3$)] [Ir(cod){MeIm(CH$_2$)$_3$SO$_3$}] (**3-Ir**) were prepared, from precursors **1** and **3**, respectively, following the general procedure entailing the reaction of the imidazolium salts with 0.5 equivalents of [Ir(μ-OMe)(cod)]$_2$ in THF at room temperature. In the case of **3-Ir** the addition of 1 equiv. of NaH as external base was required (Scheme 3). The new Ir^I-NHC complexes were isolated as yellow solids in good yields and characterized using standard spectroscopic techniques.
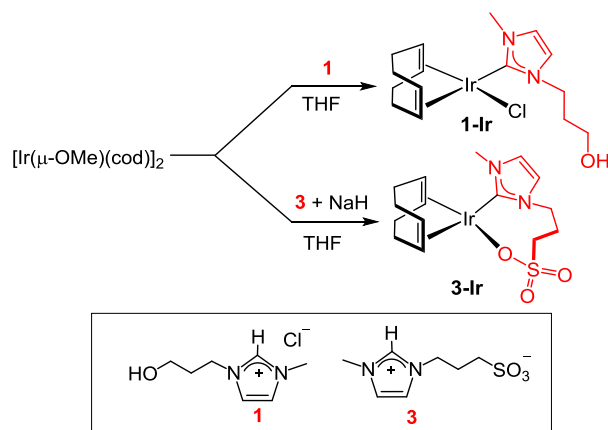
Scheme 3. Synthesis of Ir[I]-NHC complexes **1-Ir** and **3-Ir**.

The ^{1}H NMR spectra of **1-Ir** and **3-Ir** confirm the deprotonation of the imidazolium fragment, and in consequence, the expected coordination of the NHC ligand to the iridium center what becomes evident in the ^{13}C{^{1}H} NMR spectra with the characteristic upfield resonances for the carbenic carbon atom of the imidazol-2-ylidene ring at δ 180.2 ppm (**1-Ir**) and 182.5 ppm (**3-Ir**). These chemical shifts lie in the usual range for related Ir[I]-NHC complexes.[50,51] In accordance with the proposed structure, the NMR spectra of the complexes showed four resonances for the =CH olefinic protons of the cod ligand, both in the ^{1}H and in the ^{13}C{^{1}H} NMR spectra, due to the lack of an effective symmetry plane in the molecules, probably as a result of the hindered rotation around the carbene-iridium bond in the unsymmetrical NHC ligands.[52] As a consequence, the >CH$_2$ protons of the alkyl chain in both compounds are diastereotopic showing six distinct resonances that have been unequivocally assigned to their corresponding carbons with the help of the 2-D ^{1}H-^{13}C HSQC NMR spectra (see Supporting Information).

Additionally, molecular mass was guessed by means of mass spectra giving a peak at m/z ratio of 441.2 for **1-Ir**, which corresponds to the molecular ion without the chlorido ligand, and at m/z ratio of 527.4 for **3-Ir** which corresponds to the molecular ion plus a sodium cation. Both complexes are neutral as was evidenced by the conductivity measurements in

acetone or methanol and thus, the charge in **1-Ir** or **3-Ir** is compensated by the chlorido ligand and the sulfonate group, respectively. On the other hand, the solid state IR spectrum of **3-Ir** shows two strong bands at 1185 and 1042 cm^{-1}, which we attribute to the ν asymmetric and symmetric S=O stretching bands, respectively, of the coordinated sulfonate group.[53] All these gathered information allows proposing that the sulfonate group is coordinated to the metal center which is in contrast with the results in the EXAFS analysis for the related **CNT-2-Ir** material.

Water Oxidation Catalytic Activity

CAN-driven Water Oxidation Catalysis

The CNT-based Ir^{I}-NHC hybrid catalysts, **CNT-1-Ir** and **CNT-2-Ir**, are active in water oxidation catalysis. The catalytic reactions were performed on a X102 kit micro-reactor equipped with a pressure transducer which allows the measurement of O$_2$(g) evolution following the protocol described in detail in the Experimental section. Briefly, the glass vessel was charged with the solid hybrid catalyst, and once the pressure was stabilized, 2 mL of 0.400 M acidic water-solution (0.1 M HNO$_3$, pH = 1) of the sacrificial oxidant (NH$_4$)$_2$Ce(NO$_3$)$_6$ (CAN) was injected under argon atmosphere. The oxygen evolution was measured until constant pressure.

All the catalytic tests showed immediate oxygen evolution therefore, no induction period was observed, even at low catalyst loading with higher [CAN]/[Ir] ratios. Table 1 summarizes the results of CAN-driven water oxidation catalytic experiments including the number of mmol of produced O$_2$(g), TON number expressed as mmol of O$_2$(g)/mmol of iridium in the hybrid catalyst, TOF$_{50}$ and average TOF. The reaction yield was estimated relative to the maximum theoretical amount of produced O$_2$(g), 0.2 mmol, based on sacrificial oxidant. Roughly, a 70% yield was achieved with a [CAN]/[Ir] ratio of 250 (entry 1) for catalyst **CNT-1-Ir**.

Remarkably, the reaction yield increases by reducing the hybrid catalyst loading reaching to almost full conversion for [CAN]/[Ir] ratios of 600-1000 (entries 8 and 9), but only for catalyst **CNT-2-Ir**. Oxygen evolution rates are faster for catalyst **CNT-2-Ir** than for **CNT-1-Ir** (Figure 3) what could be related to the higher hydrophilicity of the former due to the presence of the propyl-sulfonate wingtip at the NHC ligand. In fact, the maximum yield attained wit catalyst **CNT-1-Ir** was 87 %. The increase of the catalyst loading resulted in faster reactions although oxygen evolution stops before reaching the maximum conversion as evidenced by the plateau in the O_2 evolution plots represented in Figure 4 which has been attributed by some authors to catalyst deactivation prior to exhausting all of the sacrificial oxidant (CAN) present in the reaction media.[54] However, these solutions showed catalytic activity after successive additions of CAN once oxygen evolution stops, which points out to a likely Ir/Ce dinuclear resting state of the catalyst that becomes activated upon addition of an excess of CAN.[55,56]
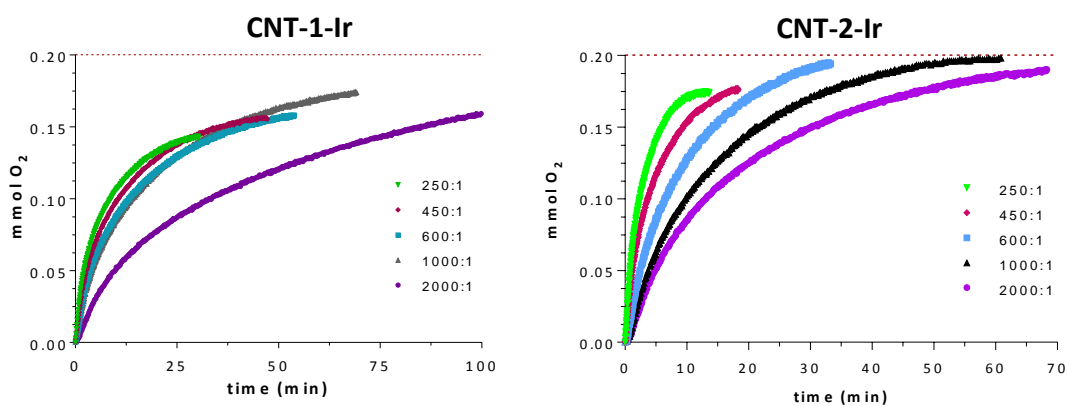

Figure 3. Plot of $O_2(g)$ evolution *vs.* time at various [CAN]/[Ir] ratios. The produced oxygen in all the catalytic tests is consistent with the stoichiometric limit of added CAN (2 mL, 0.40 M; 0.2 mmol of O_2 horizontal line).

Table 1. Influence of the [CAN]/[Ir] ratio in CAN-driven water oxidation by hybrid catalysts **CNT-1-Ir** and **CNT-2-Ir**.[a]

Entry	Cat.	mg Cat.	$[Ce^{IV}]/[Ir]^b$	mmol O_2	TON	TOF_{50} $(h^{-1})^c$	TOF $(h^{-1})^d$	yield (%)
1	**CNT-1-Ir**	6.13	250	0.142	45	220	90	70
2	**CNT-1-Ir**	3.38	450	0.156	90	320	110	78
3	**CNT-1-Ir**	2.54	600	0.158	115	330	130	79
4	**CNT-1-Ir**	1.52	1000	0.174	220	540	190	87
5	**CNT-1-Ir**	0.78	2000	0.172	420	445	175	86
6	**CNT-2-Ir**	7.12	250	0.174	55	780	290	87
7	**CNT-2-Ir**	3.88	450	0.176	100	970	330	88
8	**CNT-2-Ir**	2.98	600	0.194	140	720	275	97
9	**CNT-2-Ir**	1.78	1000	0.198	240	750	250	99
10	**CNT-2-Ir**	0.88	2000	0.190	470	1140	400	95

[a] Reactions were carried out in 2.0 mL of a 0.400 M solution of CAN in acid-buffered degassed water (0.1 M HNO_3, pH = 1) in a thermostatic bath at 298.1 K. [b] [CAN]/[Ir] ratios referenced to ICP-based %Ir content. [c] TOF_{50} values (h^{-1}) were calculated at reaction times when the number of mmol of produced $O_2(g)$ reached half of the theoretically calculated. [d] Average turnover frequency (h^{-1}) calculated at reaction time when oxygen evolution stops.

The performance of the hybrid catalysts in water oxidation has been compared with that of homogeneous iridium(I) complexes having related functionalized-NHC ligands [IrCl(cod){MeIm(CH_2)_3OH}] (**1-Ir**) and [Ir(cod)(MeIm(CH_2)_3SO_3)] (**3-Ir**). Unfortunately, we were unable to prepared the corresponding Ir^I-NHC complex from the doubly functionalized imidazolium salt [HO(CH_2)_2ImH(CH_2)_3SO_3] (**2**) which prevents a straightforward comparison with **CNT-2-Ir**. Both homogeneous catalysts exhibited a slightly superior performance than the related hydrid catalysts. Remarkably, catalyst **3-Ir** bearing a sulfonate-functionalized NHC ligand is more active than **1-Ir** what correlates with the observed for the related heterogeneous catalysts. Maximum TOF_{50} (h^{-1}) numbers of 1375 and 2300 were reached at $[Ce^{IV}]/[Ir]$ ratios of 500 and 1600 for **1-Ir** and **3-Ir**, respectively (see Supporting Information). The plot of $O_2(g)$ evolution *vs.* time for the four catalysts, Figure 4, evidences the superior catalytic performance of **3-Ir** and **CNT-2-Ir** compared to **1-Ir** and

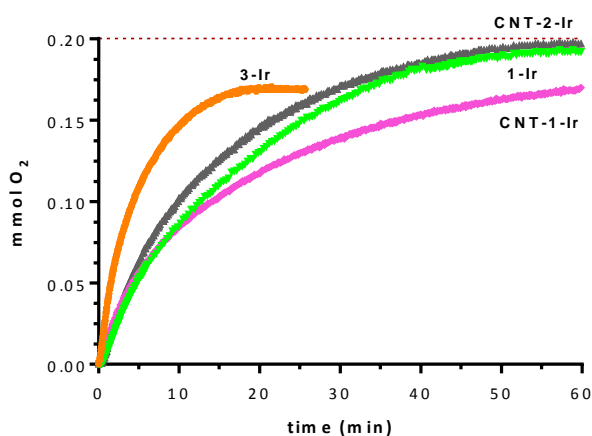**CNT-1-Ir**, what invokes again to a positive effect of the sulfonate group in the activity of the catalysts.

Figure 4. Plot of O_2(g) evolution *vs.* time for **1-Ir**, **3-Ir**, **CNT-1-Ir** and **CNT-2-Ir** at [CAN]/[Ir] ratio of 1000 except for **3-Ir** that a ratio of 800 was used (2 mL of CAN 0.400 M, horizontal line max. O_2, 0.20 mmol).

Recycling studies have been carried out with the heterogeneous catalyst **CNT-2-Ir** using the optimun [CAN]/[Ir] ratio of 1000 found in the catalytic tests. Two different types of experiments have been performed: a) multi-step CAN-driven water oxidation by successive additions of 2 mL of CAN solution (0.400 M) after oxidant consumption, and b) recovering of the hybrid catalyst at the of the reaction. In this case, the residual black solids obtained after catalysis were separated by centrifugation, washed with fresh water (2 x 5 mL) and then subjected to another catalytic cycle by addition of further 2 mL of CAN solution. The recycling performance of catalyst **CNT-2-Ir** with both procedures is illustrated in Table 2 and Figure 5.

Multi-step water oxidation experiments showed a steady decrease in the catalytic activity after two successive CAN additions as evidenced by the decrease of TOF_{50} values (Table 2). Quantitative reaction yields were attained at increasing reaction times with very similar

reaction profiles. The decrease in the catalytic activity is clearly evidenced by comparison the slope of the successive oxygen evolution plots (Figure 5a). On the other hand, recovering of the hybrid catalyst and recycling gave similar results also with an evident steady decrease in the catalytic activity (Figure 5b). Interestingly, no induction periods were observed in the recycling tests with both methods which suggest that the pre-catalyst is fully transformed into the active species after the first catalytic run.

Table 2. Recyclability and stability studies for the hybrid catalysts **CNT-2-Ir**: a) multi-step CAN-driven water oxidation, and b) recycling of the hybrid catalyst.[a]

Entry	Cat.	Test	Time[b]	mmol O_2	TON	TOF_{50} (h^{-1})[c]	TOF (h^{-1})[d]	yield (%)
a.1	**CNT-2-Ir**	fresh	31	0.196	370	1760	715	98
a.2	**CNT-2-Ir**	1st add.	37	0.194	365	1310	590	97
a.3	**CNT-2-Ir**	2nd add.	44	0.194	365	950	500	97
b.1	**CNT-2-Ir**	fresh	31	0.194	365	1760	705	97
b.2	**CNT-2-Ir**	1st cycle	39	0.186	350	1200	540	93
b.3	**CNT-2-Ir**	2nd cycle	40	0.184	345	830	515	92

[a] Reactions were carried out in 2.0 mL of a 0.400 M solution of CAN in acid-buffered degassed water (0.1 M HNO_3, pH = 1) in a thermostatic bath at 298.1 K. [b] min. [c] TOF_{50} values (h^{-1}) were calculated at reaction times when the number of mmol of produced $O_2(g)$ reached half of the theoretically calculated. [d] Average turnover frequency (h^{-1}) calculated at reaction time when oxygen evolution stops.

The gradual loss of activity observed in the recycling tests might be consequence of the detaching of the supported Ir-NHC complexes under the reactions conditions due to the presence of reactive ester linkers. CAN-driven water oxidation is performed at very strong acidic media (pH = 1) and hydrolysis of the ester linker on the nanotube wall could result in iridium leaching with loss of catalytic activity. However, the gradual degradation of the anchored molecular iridium complexes, responsible for the catalytic activity, under strong oxidizing conditions cannot be ruled out.
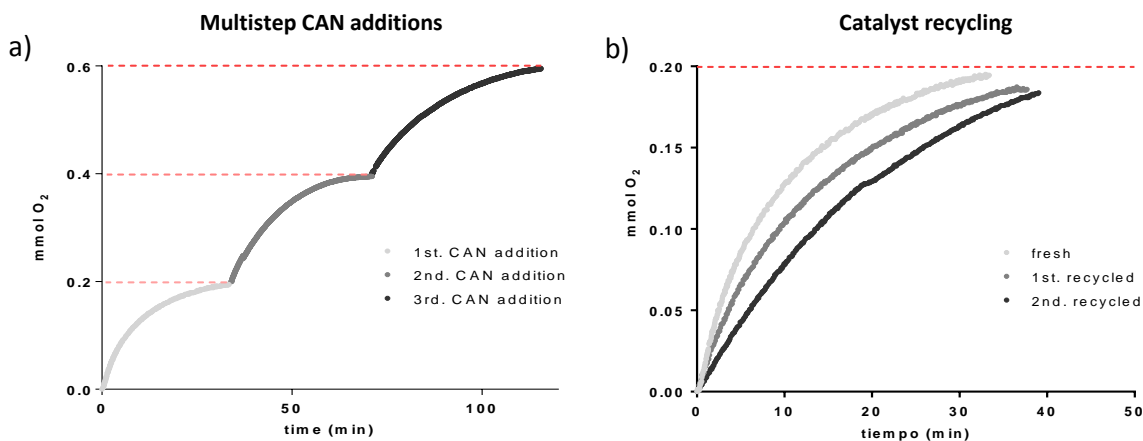
Figure 5. Recyclability and stability studies for the hybrid catalysts **CNT-2-Ir** at [CAN]/[Ir] ratio of 1000. Plots of O_2 evolution *vs.* time: a) multi-step CAN-driven water oxidation, and b) recycling of the hybrid catalyst.

As can be inferred for the activity data, the molecular catalyst precursors **1-Ir** and **3-Ir**, and the hybrid catalysts **CNT-1-Ir**, and **CNT-2-Ir** show average activities in the range of many of the iridium complexes so far reported. The activity of our homogeneous systems is comparable to that shown by the pyridine-dicarboxylate complex, [Cp*IrCl{2,6-Py(COO)(COOH)}],[57] or [Cp*IrCl{(MeIm)$_2$CHCOO}][58] (bearing a carboxylate-functionalized bis(NHC) ligand) with TOF$_{50}$ values around 1300, but also with that of the Cp*Ir^{III}-mesoinic triazolylidene-pyridine complex[59] or to the solvato complex [Cp*Ir(H$_2$O)$_3$](NO$_3$)$_2$[60] with TOF$_{50}$ values of 960 and 1260 h^{-1}, respectively; superior to that of [IrCl(cod)(ppei)] (bpi = (pyridin-2-ylmethyl)(pyridin-2-ylmethylene)amine) with TOF$_{50}$ of 372 h^{-1},[61] but lower than that shown by [Ir$_2$Cl(cod)$_2$(μ-bpi)]PF$_6$ (bpi = PyCH=NCH$_2$Py), with TOF$_{50}$ numbers up to 3400 h^{-1}.[61] As far as related heterogeneous systems tested in CAN driven water oxidation reactions, the activity is also quite similar to that shown by [Ir(Hedta)Cl]Na (Hedta = monoprotonated ethylenediaminetetraacetic acid) supported on TiO$_2$ (rutile)[62] and some Cp*Ir-pyridine-carboxylate complexes integrated in MOF structures.[63]

Electrocatalytic Water Oxidation.

Electrochemical water oxidation experiments using carbon nanotube-supported iridium-NHC materials conformed into electrodes were conducted in a standard three electrode cell using a Ag/AgCl/3.5M KCl and a graphite rod, as reference and counter electrodes respectively. A phosphate buffer solution (PBS) at a pH of 7 was selected as supporting electrolyte for the electrocatalytic tests.

The electrocatalytic water oxidation activity was firstly studied by means of cyclic voltammetry (CV) measurements (Figure 6a). The CVs were recorded between 0.00–1.40 V (*vs* Ag/AgCl/3.5M KCl, i.e., 0.20 V *vs* NHE) at pH ≈ 7.0. The catalytic currents were measured at 1.40 V which corresponds to over potential of 0.79 V over the thermodynamic potential for water oxidation (which is 0.61 V vs Ag/AgCl/3.5 M KCl at pH 7). The catalyst loadings in the two electrodes tested, **CNT-1-Ir-EC** and **CNT-2-Ir-EC**, calculated by ICP/MS were similar being 0.0026 ± 0.0001 and 0.0024 ± 0.0001 mmol/cm^2, respectively. In these conditions, a higher oxidation current density was measured on the **CNT-2-Ir-EC** electrode (≈ 59 mA/cm^2) being almost double than that on **CNT-1-Ir-EC** (≈ 28 mA/cm^2). The current densities of the neat CNTs and the background were almost negligible at this potential (≈ 1.5 and 1.1 mA/cm^2, respectively), demonstrating that the observed electrocatalytic activity can be mainly attributed to the iridium active material. In any case, a possible synergistic effect of the carbon surface in the catalytic cycle is not discarded. Interestingly, the potential at which the current start to increase during the oxidation on **CNT-2-Ir-EC** is much lower than the observed for **CNT-1-Ir-EC** which suggests that not only the catalytic reaction is more favored on **CNT-2-Ir** but this electrode also allows the more effective utilization of lower potentials.

The turnover frequencies (TOFs) were calculated on the basis of the currents measured at 1.40 V, after subtracting the background and assuming 100% of faradaic efficiency (see

Supporting Information). Thus, the calculated TOF for **CNT-2-Ir-EC** was 22000 h^{-1} which is almost double than the value of 10900 h^{-1} calculated for **CNT-1-Ir-EC**. These values are in the range of those reported for other iridium/carbon-supported hybrid catalysts,[24,63] which confirms the efficiency of the new Ir-NCH complexes supported onto CNTs as electrocatalysts for water oxidation. In addition, a positive impact of the water soluble NHC ligand in the electrocatalytic activity is observed.

As a rough estimation of the catalytic activity under both chemical and electrochemical conditions, electrocatalytic TOF values were estimated at 0.55 V (that is 1.16 V *vs* Ag/AgCl/3.5M KCl) which corresponds to the theoretical overpotential used in the Ce^{4+}-driven water oxidation at pH 1 (since the thermodynamic potentials for Ce^{4+} reduction and H$_2$O oxidation at pH 1 are 1.52 and 0.97 V (*vs* Ag/AgCl/3.5M KCl), respectively.[24] The calculated values are 13000 and 2500 h^{-1} for **CNT-2-Ir-EC** and **CNT-1-Ir-EC**, respectively, what are much larger than those measured in CAN-driven water oxidation catalytic tests for 1 h (Table 1). This demonstrates the improved performance of the conformed supported catalysts under electrochemical conditions. Moreover, this procedure also allows carrying out water oxidation catalytic studies under more environmentally friendly conditions of neutral pH where the molecular complexes are supposed to be more stable.

The stability of the electrodes was tested by means of chronoamperometry measurements (CA, Figure 6b). The CAs show a slight decay of the current measured on both electrodes, being more pronounced in the case of the **CNT-1-Ir-EC** after 2000 s of water oxidation. The evolution of oxygen during the electrocatalytic experiments follows a similar trend as confirmed by gas chromatography (Figure 6b, inset). These results confirm that the introduction of water soluble ligands in the coordination sphere of the iridium center in the hybrid catalysts do not only increases the catalytic efficiency but also its electrochemical stability.
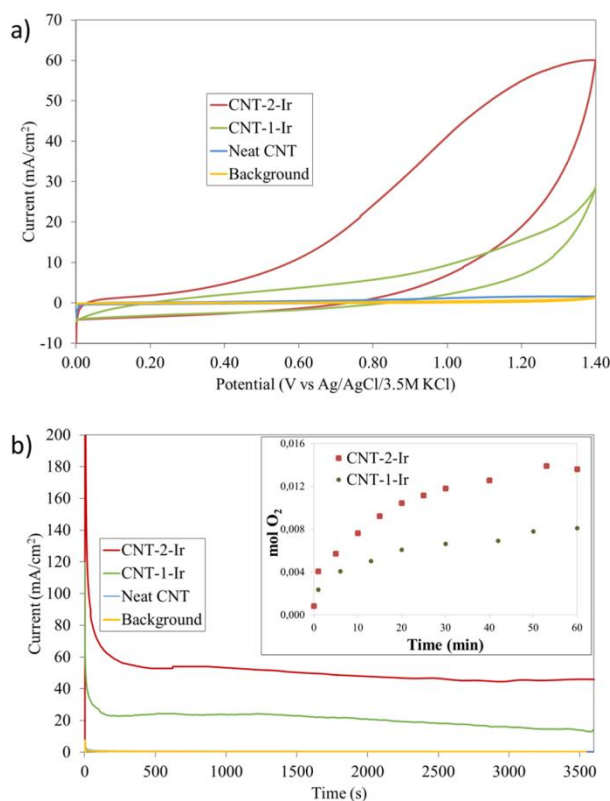
Figure 6. (a) CVs and (b) CAs recorded on **CNT-1-Ir-EC** and **CNT-2-Ir-EC** electrodes, and neat CNTs. The CV recorded on the raw graphite disk has been included for comparative purposes as the background current density. Inset in b shows the evolution of oxygen as a function of time during the chronoamperimetric measurements for catalysts **CNT-1-Ir-EC** and **CNT-2-Ir-EC**, measured by gas chromatography. CVs were recorded at a scan rate of 20 mV/s at pH 7. CAs were recorded at an applied potential of 1.40 V (vs the reference electrode) for 1 h.

The catalyst loadings remaining after 1 h of applied potential, determined by ICP/MS, were 0.0015 ± 0.0005 and 0.0022 ± 0.0007 mmol/cm^2 for **CNT-1-Ir-PEC** and **CNT-2-Ir-PEC,** respectively. At that time, TOF values of 14800 h^{-1} and 3600 h^{-1} were measured for **CNT-2-Ir-PEC** and **CNT-1-Ir-PEC**, respectively. These values, although higher than the obtained under CAN-driven water oxidation conditions, are in line of a loss of catalytic activity with time (33% for **CNT-2-Ir-EC**, and 67% for **CNT-1-Ir-EC**) what might be related to a loss of

iridium catalyst from the CNT-based electrodes. Anyhow, a small portion of carbonaceous material in suspension was detected after 1 h of electrocatalysis in both tests, although this effect more pronounced in the case of the **CNT-1-Ir** electrode. Therefore, we hypothesize that the loss of current with time might be associated with the instability of the electrode material itself rather that, or in combination with, the hydrolysis of ester linker of the iridium complex from the surface of the CNT. As an overall result, a higher stability of the CNT/iridium linker in this type of catalysis seems to be desirable. It is worth of mention that a similar behavior was already observed for other types of iridium catalyst as a consequence of the inhibition of the intermolecular decomposition pathways.[24]

Analysis of post-catalysis materials.

With the aim to elucidate the structural differences in the materials after WO catalysis, the hybrid catalysts after three CAN-driven WO catalytic cycles (**CNT-1-Ir-PC** and **CNT-2-Ir-PC**) and after 1 h of WO chronoamperometry (**CNT-1-Ir-PEC** and **CNT-2-Ir-PEC**) were examined by means of XPS and compared with those analyses of the original supported materials (**CNT-1-Ir** and **CNT-2-Ir**). The Ir4f XPS profiles and multiple peak fit values are composed by the expected two peaks due to $4f_{7/2}$-$4f_{5/2}$ doublet separation of *ca.* 3 eV (Figure 7a for **CNT-1-Ir**, Figure 7b for **CNT-2-Ir**). In spite of the XPS signal low resolution in the materials used for water oxidation catalysis driven by CAN, especially in **CNT-1-Ir-PC** what is probably due to a much lower iridium load, the shift towards higher binding energies of the two maxima of the Ir4f XPS curves of both hybrid catalysts after the two different water oxidation catalysis treatments becomes evident (Table 3).

In general, small differences of *ca.* 0.2-0.4 eV can be seen between the fresh samples and post-catalysis (PC and PEC) materials. Higher energy values were generally observed for post-catalysis materials, except for the case of **CNT-1-Ir-PC** where almost the same value was observed for the $4f_{5/2}$ peak. This is not reliable as this measurement has a bit too much of

background noise. These shifts in the XPS spectra of Ir4f double lines might be indicative of the presence of higher oxidation iridium species in the recovered WO post-catalysis materials. In fact, these correlations have already been used as evidences to support the formation of the high-valent oxo-hydroperoxo and peroxo-species in the WO processes.[64]
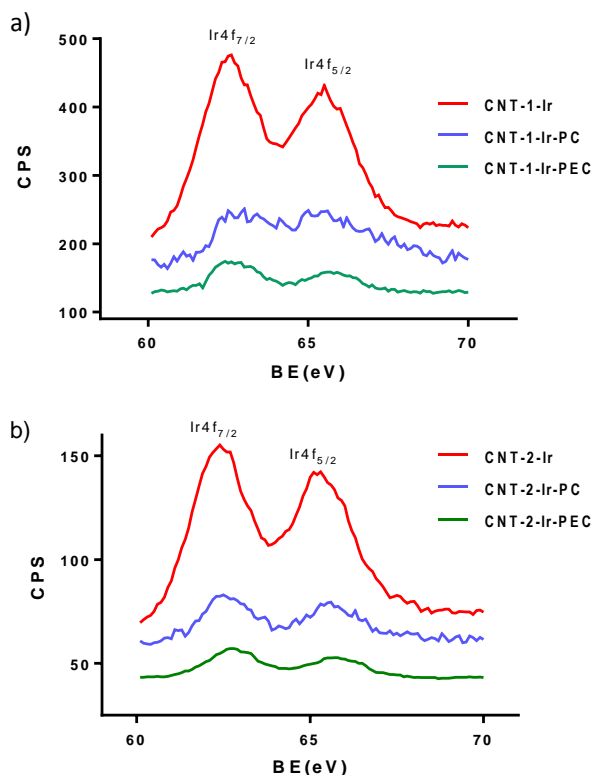

Figure 7. Ir4f XPS curves of the carbon nanotube-based Ir-NHC hybrid catalysts **CNT-1-Ir** (a) and **CNT-2-Ir** (b) fresh and post-catalysis: CAN-driven catalysis (PC) and electrocatalysis (PEC).

Table 3. Maxima, areas and widths for the two peaks $4f_{7/2}$ and $4f_{5/2}$ from the Ir4f XPS experiments (see Figure 7).

Entry	Material	$4f_{7/2}$ peak			$4f_{5/2}$ peak		
		Centre	Area	Width	Centre	Area	Width
1.	**CNT-1-Ir**	62.4(1)	508(5)	1.66(2)	65.3(1)	486(6)	2.00(3)
2	**CNT-1-Ir-PC**	62.6(1)	78(11)	1.2(1)	65.4(1)	288(27)	3.50(3)
3	**CNT-1-Ir-PEC**	62.6(1)	81(2)	1.45(3)	65.7 (1)	59(2)	1.70(1)

4	**CNT-2-Ir**	62.4(1)	153(2)	1.53(2)	65.3(1)	150(2)	1.86(3)
5	**CNT-2-Ir-PC**	62.6(1)	35(1)	1.37(4)	65.6(1)	33(1)	1.70(1)
6	**CNT-2-Ir-PEC**	62.8(1)	25.4(3)	1.51(2)	65.7(1)	19.2(3)	1.64(1)

The material **CNT-2-Ir-PC** could be also studied by an EXAFS analysis. The k^2-weighted EXAFS signal for this material shows oscillations comparable to those exhibited by the fresh **CNT-2-Ir** catalyst at low k, but the EXAFS signal decays faster at high k and has a poor quality above ~11 Å^{-1} suggesting an increase of local structural disorder respect to **CNT-2-Ir** material (see inset of Figure 8). For this reason, the analysis for these samples was limited up to $k = 11.5$ Å^{-1}. Figure 8 shows the Fourier transform (FT) of the EXAFS spectra for both materials. In both cases a prominent peak marks the contribution from the first coordination shell but two features should be noted. First of all, the main peak of **CNT-2-Ir-PC** is less intense and broader than that of **CNT-2-Ir**. The decrease of the intensity for the first peak in the FT of the post-catalysis material can be caused by either a decrease in the iridium coordination number or an increase of the local disorder around it. The fact that **CNT-2-Ir** and **CNT-2-Ir-PC** materials have similar oscillations in their EXAFS spectra but higher attenuation for the latter sample points to a higher structural disorder for **CNT-2-Ir-PC** sample in the first coordination shell. Secondly, the peak is shifted to lower R-values for **CNT-2-Ir-PC** material indicating shorter bond lengths in this compound. Therefore, accurate fits can be obtained for the first shell of both samples using the same model (Figure 8 and Table S3). The complete analysis including paths up to 3.75 Å can be consulted in the Supporting Information. Therefore, our fits confirm a higher structural disorder for **CNT-2-Ir-PC** reflected in higher Debye-Waller factors for the interatomic distances and shorter Ir-O and Ir-C bond lengths. This result suggests an increase in the oxidation state of iridium atoms in **CNT-2-Ir-PC** in agreement with the trend observed in XPS measurements (shift to higher energies of the peaks of **CNT-2-Ir-PC** spectrum respect to the ones for the fresh compound).

However, the comparison of the EXAFS spectra of **CNT-2-Ir-PC** with that of IrO_2 showed larger differences which indicates that $Ir^{IV}O_2$ particles are not present in the **CNT-2-Ir-PC** material (see Supporting Information).
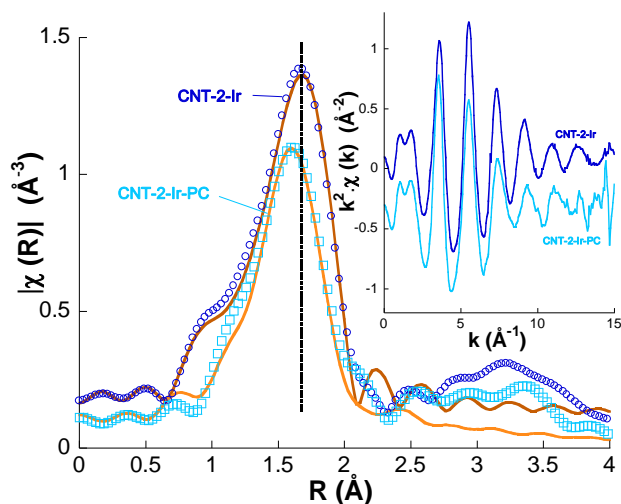

Figure 8. Comparison between experimental data (points) and best fits (solid lines) for the moduli of the FTs of the $k^2\chi$(k) EXAFS signals for **CNT-2-Ir** (circles) and **CNT-2-Ir-PC** (squares) in the R-range between 1.0 and 2.1 Å, and in the k-range between 2.0 and 11.5 Å^{-1}. The dotted line is an eye guide. Inset: $k^2\chi(k)$ EXAFS signals for both hybrid catalysts.

According to the similarity of the oxygen evolution profiles of CAN-driven water oxidation catalysis for both homogeneous and heterogeneous catalysts, and the information gathered from XPS and EXAFS characterization for the heterogeneous materials, we tentatively envisage a mechanism involving $Ir^{III}/Ir^{IV}/Ir^{V}$ intermediate species stabilized by the sulfonate-functionalized NHC ligand similar to the proposed by Crabtree[9] and Hetterscheid[65] for Cp*Ir^{III} catalysts. Assuming a Ir^{III}-H_2O species as the catalytic active species, two consecutive proton-coupled electron transfer (PCET) steps should result in the formation of an oxo [Ir^{V}=O] intermediate which could react with water, through a water nucleophilic attack mechanism, leading to an hydroperoxo [Ir^{III}-OOH] species. Two successive PCET

steps should lead to the key peroxo $[Ir^V(\eta^2-O_2)]$ intermediate from which an $O_2(g)$ molecule is released with regeneration of the catalytic active species.

CONCLUSIONS

This work demonstrates that hybrid CNT-based materials having Ir^I-NHC complexes anchored to the carbon nanotubes through ester functions are suitable as water oxidation catalysts under chemical and electrochemical conditions. The study has revealed that both heterogeneous and homogeneous molecular catalysts featuring a water soluble sulfonate-functionalized NHC ligand are much more active than related catalysts having unfunctionalized NHC ligands either in CAN-driven or electrochemical water oxidation conditions.

Despite the lower catalytic activity of the hybrid catalysts with respect to homogeneous related systems, the productivity of the heterogeneous catalysts has been improved by allowing successive CAN additions or, at least, three WOC recycling experiments. The gradual decrease in the catalytic activity along the recycling tests could be ascribed to the degradation of the anchored molecular iridium complexes or the hydrolysis of the ester linker under the hard oxidant and acidic reaction conditions. Noteworthy, the electrochemical water oxidation of CNT-based hybrid materials resulted much more efficient, with TOF values at 1.4 V up to 22000 h^{-1} for the hybrid sulfonate-functionalized catalyst.

The local structure of the iridium centers in the hybrid catalysts has been probed by EXAFS spectroscopy, before and after the chemical and electrochemical WO catalytic reactions. The first coordination shell around iridium atom is similar in both fresh specimens, corresponding to five C atoms and one O atom from the CNT wall, losing the coordination of the chlorido or the sulfonate ligand. The two main differences between fresh and post-

catalytic materials are on the one hand, an increase of local disorder in the post-catalysis material which reveals a messier environment around iridium atoms, and on the other, shorter bond lengths. The latter indicates an increase in the oxidation state of iridium atoms that can be correlated to the observed peaks shifts in the XPS spectra. Nevertheless, EXAFS spectroscopy rules out the significant presence of $Ir^{IV}O_2$ particles in this particular system.

The enhanced chemical and electrochemical water oxidation catalytic activity of the hybrid catalyst having iridium complexes based on sulfonate-functionalized NHC ligands covalently attached to carbon nanotubes is remarkable. These supported materials not only double the TOF values of the homologous less polar materials lacking a sulfonate moiety but also increases their long-term electrocatalytic stability providing a useful guide for the development of new and highly efficient water oxidation catalysts.

EXPERIMENTAL SECTION

General Considerations. The iridium starting material $[Ir(\mu\text{-OMe})(cod)]_2$ was prepared according to the literature method.[66] . The imidazolium salts 1-(3-hydroxypropyl)-3-methyl-1H-imidazol-3-ium chloride, $[MeImH(CH_2)_3OH]Cl$ (**1**),[48] and 3-(3-methyl-1H-imidazol-3-ium-1-yl)propane-1-sulfonate, $[MeImH(CH_2)_3SO_3]$ (**3**),[49] were prepared from 1-methyimidazole (MeImH) using 3-chloro propanol and 1,3-propane sultone as alkylating agents. Raw CVD-grown multiwall carbon nanotubes (**CNT**) were oxidized according to the previously described procedure.[29] Solvents were distilled immediately prior to use from the appropriate drying agents or obtained from a Solvent Purification System (Innovative Technologies). $CDCl_3$, CD_3OD and acetone-d_6 were purchased from Euriso-top and used as received. All chemicals, including multiwall carbon nanotubes (MWCNT) were purchased from Aldrich and used as received except 1-methyimidazole that was distilled prior to use.

Scientific Equipment. Characterization of supports and hybrid catalysts. NMR spectra were recorded on a Bruker Advance 300 or a Bruker Advance 400 spectrometers: ^{1}H (300.1276 MHz, 400.1625 MHz) and ^{13}C (75.4792 MHz, 100.6127 MHz). NMR chemical shifts are reported in ppm relative to tetramethylsilane and referenced to partially deuterated solvent resonances. Coupling constants (*J*) are given in Hertz. Spectral assignments were achieved by combination of ^{1}H-^{1}H COSY, ^{13}C APT and ^{1}H-^{13}C HSQC experiments. MALDI-ToF mass spectra were obtained on a Bruker MICROFLEX spectrometer using DCTB (trans-2-[3-(4-tert-butylphenyl)-2-methyl-2propenylidene]malononitrile) or DIT (Ditranol) as matrixes.[67] Electrospray mass spectra (ESI-MS) were recorded on a Bruker MicroTof-Q using sodium formiate as reference. Conductivities were measured in *ca.* 5 10^{-4} M acetone solutions of the complexes using a Philips PW 9501/01 conductimeter.

Thermogravimetric analyses (TGA) were performed on a TA SDT 2960 analyzer. The procedure was as follow: 3 mg of sample was heated in the thermobalance to 1000 ºC at 10 ºC min^{-1} using a nitrogen:air flow (1:1) of 200 mL min^{-1}. High-resolution transmission electron microscopy (HRTEM) images were obtained using a JEOL JEM-2100F transmission electron microscope, equipped with a field-emission-gun (FEG) and operating at 200 kV. Energy-dispersive X-ray spectroscopy (EDX) was used to verify the atomic composition of the hybrid catalyst. Elemental analyses were performed on a LECO-CHNS-932 micro-analyser and a LECO-VTF-900 furnace coupled to the micro-analyser. X-ray photoemission spectroscopy (XPS) spectra were performed on a SPECS system operating under a pressure of 10^{-7} Pa with a Mg Kα X-ray source. The spectra did not require charge neutralization and were subsequently calibrated to the C1s line at 284.5 eV. The type of functional groups in the carbon nanotubes was quantified by deconvolution of the high resolution C1s XPS peak in Gaussian and Lorentzian functions.[68] The amount of iridium in the hybrid catalysts was

determined by means of Inductively Coupled Plasma Mass Spectrometry (ICP-MS) in an Agilent 7700x instrument.[69]

Synthesis of 3-(1-(2-hydroxyethyl)-1H-imidazol-3-ium-3-yl)propane-1-sulfonate, [HO(CH$_2$)$_2$ImH(CH$_2$)$_3$SO$_3$] (2). 2-(1*H*-imidazol-1-yl)ethan-1-ol (600 mg, 5.35 mmol) was reacted with a solution of 1-3-propanesultona (720 mg, 5.89 mmol) in acetonitrile (15 mL) for 12 h at the reflux temperature. The white solid formed was separated by decantation, washed with acetonitrile (2x5 mL) and dried in vacuum. Yield: 73%. Anal. Calcd for C$_8$H$_{14}$N$_2$O$_4$S: C, 41.01; H, 6.02; N, 11.96; S, 13.69. Found: C, 40.78; H, 6.04; N, 12.00; S, 13.78. ^{1}H NMR (298 K, CD$_3$OD): δ 9.02 (s, 1H, NCHN), 7.70 (t, J = 2.0, 1H, =CH Im), 7.65 (t, J = 2.0, 1H, =CH Im), 4.45 (t, J = 7.1, 2H, NCH$_2$, SO$_3^-$ wingtip), 4.31 (m, 2H, NCH$_2$, OH wingtip), 3.88 (m, 2H, CH$_2$OH), 2.83 (t, J = 7.0, 2H, CH$_2$SO$_3$), 2.34 (q, J_{H-H} = 7.0, 2H, CH$_2$). ^{13}C{^{1}H} NMR (298 K, MeOD): δ 138.1 (NCHN), 124.2 (=CH Im), 123.7 (=CH Im), 61.0 (CH$_2$OH), 53.4 (NCH$_2$, OH wingtip), 49.6 (NCH$_2$, SO$_3^-$ wingtip), 48.4 (CH$_2$SO$_3^-$), 27.1 (CH$_2$). MS (ESI+, MeOH) m/z = 257 [M + Na]$^+$.

Preparation of the functionalized nanotubes CNT-1 and CNT-2. The oxidized carbon nanotubes were functionalized with the imidazolium salts following a two-steps procedure. First, 0.100 g of oxidized carbon nanotubes (**CNT**) were refluxed in 40 mL of thionyl chloride for 24 h under a nitrogen atmosphere. The resultant product was washed three times with 20 mL of anhydrous tetrahydrofuran (THF) and dried for 2 h under vacuum. Then, the solids were dispersed in 15 mL of anhydrous THF and 70 mg of imidazolium salt, **1** or **2**, were added under a nitrogen atmosphere. The mixtures were refluxed for 24 h. The solids were filtered and washed with THF (3 x 20 mL), dichloromethane (3 x 20 mL) and ethanol (3 x 20 mL), and dried at 100 ºC in a preheated furnace. The samples obtained were labelled as **CNT-1**[30] and **CNT-2** for the imidazolium salts **1** and **2**, respectively. **CNT-1**: ^{1}H-PRESAT NMR (298K, acetone-d_6): δ 8.72 (m, 1H, NCHN), 7.48 (m, 2H, =CH Im), 4.32 (m, 2H, CH$_2$),

3.89 (m, 3H, CH$_3$), 3.64 (m, 2H, CH$_2$), 2.08 (m, 2H, CH$_2$). **CNT-2**: ^{1}H-PRESAT NMR (298K, D$_2$O): δ 8.88 (s, 1H, NCHN), 7.59 (m, 1H, =CH Im), 7.56 (m, 1H, =CH Im), 4.40 (t, *J* = 7.0, 2H, NCH$_2$, SO$_3^-$ wingtip), 4.34 (t, *J* = 5.1, 2H, NCH$_2$, OH wingtip), 3.94 (t, *J* = 5.1, 2H, CH$_2$OH), 2.94 (t, *J* = 7.1, 2H, CH$_2$SO$_3$), 2.34 (q, *J* = 7.0, 2H, CH$_2$).

Preparation of hybrid catalysts CNT-1-Ir and CNT-2-Ir. Functionalized carbon nanotubes **CNT-1**[30] and **CNT-2** were reacted with [Ir(μ-OMe)(cod)]$_2$ (69.6 mg, 0.105 mmol) in 10 mL of THF under an argon atmosphere. The mixture was refluxed for 2 days and then immersed into an ultrasonic bath for 30 min. The resultant solid was recovered by centrifugation, washed with THF (5 x 10 mL) and diethyl ether (2 x 5mL) and dried under vacuum.

Synthesis of [IrCl(cod){MeIm(CH$_2$)$_3$OH}] (1-Ir). [Ir(μ-OMe)(cod)]$_2$ (189 mg, 0.283 mmol) and [MeImH(CH$_2$)$_3$OH]Cl (**1**) (100 mg, 0.567 mmol) were mixed in a schlenk tube under an argon atmosphere in THF (15 mL). The mixture was stirred at room temperature for 12 h to give a solution that was concentrated under reduced pressure. The solid formed was eliminated by filtration and the resulting orange solution brought to dryness under vacuum. Treatment of the yellow residue with pentane rendered a bright yellow solid which was separated by decantation, washed with pentane, and dried in vacuum. Yield: 86%. Anal. Calcd for C$_{15}$H$_{24}$ClIrN$_2$O: C, 37.85; H, 5.08; N, 5.88. Found: C, 37.68; H, 5.03; N, 5.86. ^{1}H NMR (298 K, CDCl$_3$): δ 6.85, (q, *J* = 1.9, 2H, =CH Im), 5.22 (dd, *J* = 11.5, 4.1, 1H, NCH$_2$), 4.61, 4.54 (m, 1H each, =CH cod), 4.01 (dt, *J* = 13.8, 4.1, 1H, NCH$_2$), 3.94 (s, 3H, MeIm), 3.56, 3.47 (m, 2H, 1H each, OCH$_2$), 3.14 (m, 1H, OH), 2.98, 2.90 (m, 2H, 1H each, =CH cod), 2.22 (m, 4H, CH$_2$ cod), 2.11–1.88 (m, 2H, CH$_2$), 1.80–1.54 (m, 4H, CH$_2$ cod). ^{13}C{^{1}H} NMR (298 K, CDCl$_3$): δ 180.2 (NCN), 122.5, 119.3 (=CH Im), 85.1, 84.4 (CH cod), 56.7 (CH$_2$O), 52.5, 52.2 (CH cod), 46.1 (NCH$_2$), 37.6 (MeIm), 34.0, 33.3 (CH$_2$ cod), 32.7 (CH$_2$), 30.0, 29.4 (CH$_2$ cod). MS (MALDI-TOF, DCTB matrix, CH$_2$Cl$_2$) *m/z* = 441.2 [M − Cl]$^+$.

Synthesis of [Ir(cod){MeIm(CH$_2$)$_3$SO$_3$}] (3-Ir). [Ir(μ-OMe)(cod)]$_2$ (100 mg, 0.150 mmol) and the imidazolium salt [MeImH(CH$_2$)$_3$SO$_3$] (**3**) (60.74 mg, 0.300 mmol) were mixed in THF (10 mL) under an argon atmosphere. . Then, a solution of NaH (7.25 mg, 0.300 mmol) in a MeOH (10 mL) was slowly added and the mixture stirred at room temperature for 18 h. The suspension was concentrated until 10 mL to give a white solid that was eliminated by filtration. The resulting yellow solution was brought to dryness under vacuum and the residue disaggregated by stirring in Et$_2$O to give a bright yellow solid that was washed with Et$_2$O (3 x 2 mL) and dried under vacuum. Yield: 66%. Anal. Calcd for C$_{15}$H$_{23}$IrN$_2$O$_3$S: C, 35.77; H, 4.60; N, 5.56; S, 6.37. Found: C, 35.18; H, 4.75; N, 4.82; S, 6.44. ^{1}H NMR (298 K, CD$_3$OD): δ 7.20, 7.17 (d, J = 1.9, 1H each, =CH Im), 4.75, 4.57 (m, 2H, 1:1, NCH$_2$), 4.39, 4.29 (m, 1H each, =CH cod), 4.05 (s, 3H, NCH$_3$), 2.98 (t, J = 7.4, 2H, CH$_2$SO$_3$), 2.72, 2.61 (m, 1H each, =CH cod), 2.45 (m, 2H, >CH$_2$), 2.36–2.17 (m, 4H, CH$_2$ cod), 1.82–1.54 (m, 4H, CH$_2$ cod). ^{13}C{^{1}H} NMR (298 K, CD$_3$OD): δ 182.5 (NCN), 123.3, 121.7 (=CH Im), 84.5, 83.7 (=CH cod), 49.3 (NCH$_2$), 49.0 (CH$_2$SO$_3$), 49.6, 48.4 (=CH cod), 37.4 (CH$_3$Im), 34.8, 34.0, 30.6, 29.7 (CH$_2$ cod), 27.6 (>CH$_2$ SO$_3$). MS (ESI$^+$, MeOH) *m/z*: 527.4 [M + Na]$^+$.

Oxygen Evolution Measurements. O$_2$ evolution was dynamically monitored within pressure transductor equipped reactor (*Man on the Moon* series X102 kit micro-reactor, www.manonthemoontech.com). In a typically experiment: a 14.2 mL micro-reactor isothermal stabilized to 298 K was charged with the supported catalyst or 0.5 mL of an aqueous solution of the iridium complex under an argon atmosphere, and 2 mL of a 0.400 M water-solution of CAN (cerium ammonium nitrate) buffered in 1 M HNO$_3$. Oxygen evolution was measured until constant pressure and the amount of O$_2$(g) (mmol) produced was calculated by using the Ideal Gas Law. Each value is averaged out form at least three measurements. Samples obtained after the catalytic cycle were labeled as **CNT-1-Ir-PC** and **CNT-2-Ir-PC**.

Electrochemical measurements: Electrodes were prepared as follows: 22.5 mg of **CNT-1-Ir** or **CNT-2-Ir** (as active material) were mixed with 7.5 mg of PVFD (as binder) in an agate mortar and then put into EtOH suspension (5 mg/mL). A certain volume of each one of the previously prepared suspensions was drop-casted onto a graphite disk current collector (2 cm^2) and dried at 80 °C (1 h) in order to remove the solvent. The final amount of **CNT-X-Ir** deposited in the electrodes was 5 mg approximately. CV and CA experiments were performed in a Teflon home-made three-electrode cell (see Supporting Information) at room temperature and under inert atmosphere. The cell consisted of the previously prepared **CNT-1-Ir** and **CNT-2-Ir** electrodes as the working electrodes (1 cm^2 of exposed area), Ag/AgCl (3.5M KCl) as the reference electrode and a graphite rod as the counter electrode. All the potentials reported in this study were referenced to Ag/AgCl/3.5M KCl (i.e., 0.205 V *vs.* NHE). The supporting electrolyte consisted of a 1.0 M phosphate buffer solution (PBS) at pH 7.0. The electrochemical measurements were performed on a BioLogic VMP Multichannel Potentiostat. Samples obtained after the electrocatalytic tests were labeled as **CNT-1-Ir-PEC** and **CNT-2-Ir-PEC**. The evolution of oxygen was measured by using a HP 5890 gas chromatograph.

The TOF Turnover frequencies for the catalysis were calculated from the equation, TOF = - $(I_a . \eta)/(n.F.\gamma)$,[70] where I_a is the catalytic current density, η is the faraday efficiency, F is the Faraday´s constant, γ is the surface concentration of catalyst and n is the number of electrons transferred per production of oxygen molecule (n = 4). It was assumed that all transferred charge is used to catalyze water oxidation (η = 100%).

EXAFS measurements. Room temperature X-ray absorption measurements at the Ir L$_3$-edge were carried out using a Si (311) double crystal monochromator at the CLAESS beam line[71] of the Alba synchrotron facility (Barcelona, Spain). The energy resolution $\Delta E/E$ was estimated to be about 8×10^{-5} at the Ir L$_3$-edge, a pellet of Ir metal mixed with c[72]ellulose

was simultaneously measured for energy calibration. The Extended X-ray Absorption Fine structure (EXAFS) spectra were analyzed using the ARTEMIS program,[46] which makes use of theoretical phases and backscattering amplitudes calculated from FEFF6 code.[73] The fits were carried out in R space using a Hanning window for filtering purposes.

ASSOCIATED CONTENT

Supporting information

NMR spectra of functionalized imidazolium salts and iridium complexes, additional characterization of CNT-based materials, detailed experimental processes, and complementary catalytic results. This material is available free of charge via the Internet at http://pubs.acs.org.

AUTHOR INFORMATION

Corresponding Author

M. Victoria Jiménez: vjimenez@unizar.es, tlf: +34 876553794

Patricia Álvarez: par@incar.csic.es, tlf: +34 985118990,

Present Addresses

† Department of Chemical Sciences and INSTM Unit, University of Padova, Via F. Marzolo 1, 35131, Padova.

ORCID

M. Victoria Jiménez: 0000-0002-0545-9107

Patricia Álvarez: 0000-0001-9676-0546

Ana M. Pérez-Mas: 0000-0003-1110-2638

Zoraida González: 0000-0001-8932-3671

Beatriz Sánchez-Page: 0000-0002-2449-7459

Jesús J. Pérez-Torrente: 0000-0002-3327-0918

Javier Blasco: 0000-0002-9706-3272

Gloria Subias: 0000-0002-9029-1977

Matias Blanco: 0000-0001-7323-8149

Rosa Menéndez: 0000-0002-2670-4204

Author Contributions

The manuscript was written through contributions of all authors. All authors have given approval to the final version of the manuscript.

Notes

The authors declare no competing financial interest.

REFERENCES

(1) Li, J.; Güttinger, R.; Moré, R.; Song, F.; Wan W.; Patzke, G. R. *Chem. Soc. Rev.* **2017**, *46*, 6124–6147.

(2) Cao, R.; Laia W.; Du, P. Catalytic Water Oxidation at Single Metal Sites. *Energy Environ. Sci.* **2012**, *5*, 8134–8157.

(3) Nocera, D. G. The Artificial Leaf. *Acc. Chem. Res.* **2012**, *45*, 767–776.

(4) Concepcion, J. J.; Jurss, J. W.; Brennaman, M. K.; Hoertz, P. G.; Patrocinio, A. O. T.; Iha, N. Y. M.; Templeton, J. L.; Meyer, T. J. Making Oxygen with Ruthenium Complexes. *Acc. Chem. Res.* **2009**, *42*, 1954–1965.

(5) Fukuzumi, S.; Jung, J.; Yamada, Y.; Kojima, T.; Nam, W. Homogeneous and Heterogeneous Photocatalytic Water Oxidation by Persulfate. *Chem. Asia J.* **2016**, *11*, 1138–1150.

(6) Gust, D.; Moore, T. A. ; Moore, A. L. Solar Fuels via Artificial Photosynthesis. *Acc. Chem. Res.* **2009**, *42*, 1890–1898.

(7) Hunter, B. M.; Gray, H. B.; Müller, A. M. Earth-Abundant Heterogeneous Water Oxidation Catalysts. *Chem. Rev.* **2016**, *116*, 14120–14136.

(8) Llobet, A. *Molecular Water Oxidation Catalysis. A Key Topic for New Sustainable Energy Conversion Schemes*, Wiley: Chichester, UK, 2014.

(9) Blakemore, J. D.; Crabtree, R. H.; Brudvig, G. W. Molecular Catalysts for Water Oxidation. *Chem. Rev.* **2015**, *115*, 12974–13005.

(10) Woods, J. A.; Bernhard, S.; Albrecht, M. In *Molecular Water Oxidation Catalysis. A Key Topic for New Sustainable Energy Conversion Schemes*; Llobet, A. Ed.; Wiley: Chichester, UK, 2012; Chapter 5, pp 77−107.

(11) McDaniel, N. D.; Coughlin, F. J.; Tinker, L. L.; Bernhard S. Cyclometalated Iridium(III) Aquo Complexes: Efficient And Tunable Catalysts For The Homogeneous Oxidation Of Water. *J. Am. Chem. Soc.* **2008**, *130*, 210−217.

(12) Corbucci, I.; Macchioni, A.; Albrecht, M. In *Iridium(III) in Optoelectronic and Photonics Applications;* Zysman-Colman, E. Ed.; Wiley-VCH: Weinheim, 2017; Chapter 13, pp 617−654.

(13) Kärkäs, M. D.; Verho, O.; Johnston, E.V.; Åkermark, B. Artificial Photosynthesis: Molecular Systems for Catalytic Water Oxidation. *Chem. Rev.* **2014**, *114*, 11863−12001.

(14) Shopov, D. Y.; Sharninghausen, L. S.; Sinha, S. B.; Mercado, B. Q.; Balcells, D.; Brudvig, G. W.; Crabtree, R. H. A Dinuclear Iridium(V,V) Oxo-Bridged Complex Characterized Using a Bulk Electrolysis Technique for Crystallizing Highly Oxidizing Compounds. *Inorg. Chem.* **2018**, *57*, 5684−5691.

(15) Bofill, R.; García-Antón, J.; Escriche L.; Sala, X. Chemical, Electrochemical and Photochemical Molecular Water Oxidation Catalysts. *J. Photochem. Photobiol. B* **2015**, *152*, 71–81.

(16) Diaz-Morales, O.; Hersbach, T. J. P; Hetterscheid, D. G. H.; Reek, J. N. H.; Koper, M. T. M. Electrochemical and Spectroelectrochemical Characterization of an Iridium-Based Molecular Catalyst for Water Splitting: Turnover Frequencies, Stability, and Electrolyte Effects. *J. Am. Chem. Soc.* **2014**, *136,* 10432−10439.

(17) Zhan, S.; Ahlquist, M. S. G. Dynamics and Reactions of Molecular Ru Catalysts at Carbon Nanotube−Water Interfaces. *J. Am. Chem. Soc.* **2018**, *140,* 7498–7503.

(18) Matheu, R.; Moreno-Hernández, I. A.; Sala, X.; Gray, H. B.; Brunschwig, B. S.; Llobet, A.; Lewis, N. S. Photoelectrochemical Behavior of a Molecular Ru-Based Water-Oxidation Catalyst Bound to TiO_2-Protected Si Photoanodes. *J. Am. Chem. Soc.* **2017**, *139*, 11345–11348.

(19) Chen, Z.; Concepcion, J. J.; Jurss, J. W.; Meyer, T. J. Single-Site, Catalytic Water Oxidation on Oxide Surfaces. *J. Am. Chem. Soc.* **2009**, *131*, 15580–15581.

(20) Ashford, D. L.; Lapides, A. M.; Vannucci, A. K.; Hanson, K.; Torelli, D. A.; Harrison, D. P.; Templeton, J. L.; Meyer, T. J. Water Oxidation by an Electropolymerized Catalyst on Derivatized Mesoporous Metal Oxide Electrodes. *J. Am. Chem. Soc.* **2014**, *136*, 6578–6581.

(21) LLobet, A. Catalytic Water Oxidation: Rugged Water-Oxidation Anodes. *Nature Chem.* **2010**, *2*, 804–805.

(22) Toma, F. M.; Sartorel, A.; Iurlo, M.; Carraro, M.; Parisse, P.; Maccato, C.; Rapino, S.; González, B. R.; Amenitsch H.; Da Ros, T.; Casalis, L.; Goldoni, A.; Marcaccio, M.; Scorrano, G.; Scoles, G.; Paolucci, F.; Prato, M.; Bonchio, M. Efficient Water Oxidation At Carbon Nanotube-Polyoxometalate Electrocatalytic Interfaces. *Nat. Chem.* **2010**, *2*, 826–831.

(23) Schaetz, A.; Zeltner, M.; Stark, W. J. Carbon Modifications and Surfaces for Catalytic Organic Transformations. *ACS Catal.* **2012**, *2*, 1267−1284.

(24) deKraft, K.; Wang, C.; Xie, Z.; Su, X.; Hinds, B. J.; Lin, W. Electrochemical Water Oxidation with Carbon-Grafted Iridium Complexes. *ACS Appl. Mater. Interfaces*, **2012**, *4*, 608–613.

(25) Chen, W.; Huang, L.; Hu, J.; Li, T.; Jia, F.; Song, Y. Connecting Carbon Nanotubes to Polyoxometalate Clusters for Engineering High-Performance Anode Materials. *Phys. Chem. Chem. Phys.* **2014**, *16*, 19668–19673.

(26) Hu, B.; Wang, K.; Wu, L.; Yu, S-H.; Antonietti, M.; Titirici, M.; Engineering Carbon Materials from the Hydrothermal Carbonization Process of Biomass. *Adv. Mater.* **2010**, *22*, 813–828.

(27) Bacsa; R.R.; Laurent, C.; Peigney, A.; Bacsa, W.S.; Vaugien, T.; Rousset, A. High Specific Surface Area Carbon Nanotubes from Catalytic Chemical Vapor Deposition Process. *Chemical Physics Letters,* **2000**, *323*, 566-571.

(28) Chen, W.; Fan, Z.; Pan, X.; Bao, X. Effect of Confinement in Carbon Nanotubes on the Activity of Fischer−Tropsch Iron Catalyst *J. Am. Chem. Soc.* **2008**, *130,* 9414–9419.

(29) Blanco, M.; Álvarez, P.; Blanco, C.; Jiménez, M. V.; Pérez-Torrente, J. J.; Oro, L. A.; Blasco, J.; Cuartero, V.; Menéndez, R. Enhancing the Hydrogen Transfer Catalytic Activity of Hybrid Carbon Nanotube-Based NHC-Iridium Catalysts by Increasing the Oxidation Degree of the Nanosupport. *Catal. Sci. Technol.* **2016**, *6*, 5504–5514.

(30) Blanco, M.; Álvarez, P.; Blanco, C.; Jiménez, M. V.; Blasco, J; Pérez-Torrente, J. J.; Oro, L. A.; Menéndez, R. Enhanced Hydrogen-Transfer Catalytic Activity of Iridium N-Heterocyclic Carbenes by Covalent Attachment on Carbon Nanotubes. *ACS Catal.* **2013**, *3*, 1307–1317.

(31) Avilés, F.; Cauich-Rodríguez, J. V.; Moo-Tah, L.; May-Pat, A.; Vargas-Coronado, R. Evaluation of Mild Acid Oxidation Treatments for MWCNT Functionalization. *Carbon* **2009**, *47*, 2970–2975.

(32) Solvent Suppression using TopSpin 3.x: https://www.bruker.com/products/mr/nmr/nmr-software/nmr-software/topspin.

(33) Chiang, Y. C.; Lin, W. H.; Chang, Y. C. The Influence of Treatment Duration on Multi-Walled Carbon Nanotubes Functionalized by H_2SO_4/HNO_3 Oxidation. *Appl. Surf. Sci.* **2011**, *257*, 2401–2410.

(34) Kannan, A. G.; Zhao, J.; Jo, S. G.; Kang, Y. S.; Kim, D. Nitrogen and Sulfur Co-Doped Graphene Counter Electrodes Wwith Synergistically Enhanced Performance for Dyesensitized Solar Cells. *J. Mater. Chem. A* **2014**, *2*, 12232–12239.

(35) Park, M. J.; Lee, J. K.; Lee, B. S.; Lee, Y. W.; Choi, I. S.; Lee, S. Covalent Modification of Multiwalled Carbon Nanotubes with Imidazolium-Based Ionic Liquids: Effect of Anions on Solubility. *Chem. Mater.* **2006**, *18*, 1546–1551.

(36) Baskaran, D.; Mays, J. W.; Bratcher, M. S. Polymer-Grafted Multiwalled Carbon Nanotubes through Surface-Initiated Polymerization. *Angew. Chem. Int. Ed.* **2004**, *43*, 2138–2142.

(37) Abou-Hamad, E.; Babaa, M.-R.; Bouhrara, M.; Kim, Y.; Saih, Y.; Dennler, S.; Mauri, F.; Basset, J.-M.; Goze-Bac, C.; Wågberg, T. Structural Properties of Carbon Nanotubes Derived from ^{13}C NMR. *Physical Rev. B* **2011**, *84*, 165417(6).

(38) Blasco, J.; Cuartero, V.; Subías, G.; Jiménez, M. V; Pérez-Torrente, J. J.; Oro, L. A.; Blanco, M.; Álvarez, P.; Blanco, C.; Menéndez, R. Local Structure of Iridium Organometallic Catalysts Covalently Bonded to Carbon Nanotubes. *J. Phys. Conf. Ser.* **2016**, *712*, 12052(4).

(39) Fritsch. A.; Légaré, P. XPS Study of Small Iridium Clusters; Comparison with the $Ir_4(CO)_{12}$ Molecule. *Surf. Sci.* **1984**, *145*, L517–L523.

(40) Zahmakiran M. Iridium Nanoparticles Stabilized by Metal Organic Frameworks (IrNPs@ZIF-8): Synthesis, Structural Properties and Catalytic Performance. *Dalton Trans.* **2012**, *41*, 12690–12696.

(41) Uzun, A.; Ortalan, V.; Browning, N. D.; Gates, B. C. A site-isolated mononuclear iridium complex catalyst supported on MgO: Characterization by spectroscopy and aberration-corrected scanning transmission electron microscopy. *J. Catal.* **2010**, *269*, 318–328.

(42) Lu, J.; Serna, P.; Aydin, C.; Browning, N. D.; Gates, B. C. Supported Molecular Iridium Catalysts: Resolving Effects of Metal Nuclearity and Supports as Ligands. *J. Am. Chem. Soc.* **2011**, *133*, 16186–16195.

(43) Blanco, M.; Álvarez, P.; Blanco, C.; Jiménez, M. V.; Fernandez-Tornos, J.; Pérez-Torrente, J. J.; Blasco, J; Subías, G.; Cuartero, V.; Oro, L. A.; Menéndez, R. Effect of Structural Differences of Carbon Nanotubes and Graphene Based Iridium-NHC Materials on the Hydrogen Transfer Catalytic Activity. *Carbon* **2016**, *96*, 66–74.

(44) Crotti, C.; Farnetti, E.; Filipuzzi, S.; Stener, M.; Zangrando. E.; Moras, P. Evaluation of the Donor Ability of Phenanthrolines in Iridium Complexes by Means of Synchrotron Radiation Photoemission Spectroscopy and DFT Calculations. *Dalton Trans.* **2007**, 133–142.

(45) Louw, W. J.; De Waal, D. J. A.; Gerber, T. I. A.; Demanet, C. M.; Copperthwaite, R. G. Reaction of Small Molecules with Low-Valent Metal Complexes: Addition or Oxidative Addition? *Inorg. Chem.* **1982**, *21*, 1667–1668.

(46) Ravel, B.; Newville, M. ATHENA, ARTEMIS, HEPHAESTUS: Data Analysis for X-ray Absorption Spectroscopy Using IFEFFIT. *J. Synchrotron Radiat.* **2005**, *12*, 537–541.

(47) Wang, C. -Q; Lewis, A. R.; Batchelor, R. J.; Einstein, F. W. B.; Willner, H.; Aubke, F. Synthesis, Molecular Structure, and Vibrational Spectra of mer-Tris(carbonyl)iridium(III) Fluorosulfate, mer-Ir(CO)$_3$(SO$_3$F)$_3$. *Inorg. Chem.* **1996**, *35*, 1279–1285.

(48) Bekhouche, M.; Blum, L. J.; Doumèche, B. Ionic Liquid-Inspired Cations Covalently Bound to Formate Dehydrogenase Improve its Stability and Activity in Ionic Liquids. *ChemCatChem* **2011**, *3*, 875–882.

(49) Azúa, A.; Sanz, S.; Peris, E. Sulfonate-Functionalized NHC-Based Ruthenium Catalysts for the Isomerization of Allylic Alcohols in Water. Recyclability Studies. *Organometallics* **2010**, *29*, 3661–3664.

(50) Puerta-Oteo, R.; Jiménez, M. V.; Lahoz, F. J.; Modrego, F. J.; Passarelli V.; Pérez-Torrente J. J. *Inorg. Chem.*, 2018, **57**, 5526–5543.

(51) Sipos, G.; Dorta, R. Iridium Complexes with Monodentate N-Heterocyclic Carbene Ligands. *Coord. Chem. Rev.* **2018**, *375*, 13–68.

(52) Enders, D.; Gielen, H. Synthesis of Chiral Triazolinylidene and Imidazolinylidene Transition Metal Complexes and First Application in Asymmetric Catalysis. *J. Organomet. Chem.* **2001**, *617–618*, 70–80.

(53) White, N. G.; Feltham, H. L. C.; Gandolfi, C.; Albrecht, M.; Brooker, S. Towards Langmuir–Blodgett films of magnetically interesting materials: solution equilibria in amphiphilic iron(II) complexes of a triazole-containing ligand. *Dalton Trans.* **2010**, *39*, 3751–3758.

(54) Li, M.; Takada, K.; Goldsmith, J. I.; Bernhard, S. Iridium(III) Bis-Pyridine-2-Sulfonamide Complexes as Efficient and Durable Catalysts for Homogeneous Water Oxidation. *Inorg. Chem.* **2016**, *55*, 518–526.

(55) Bucci, A.; Menendez Rodriguez, G.; Bellachioma, G.; Zuccaccia, C.; Poater, A.; Cavallo, L.; Macchioni, A. An Alternative Reaction Pathway for Iridium-Catalyzed Water Oxidation Driven by Cerium Ammonium Nitrate (CAN). *ACS Catal.* **2016**, *6*, 4559–4563.

(56) Codolà, Z.; Gómez, L.; Kleespies, S. T.; Que, L.; Costas, M.; Lloret-Fillol, J. Evidence for an Oxygen Evolving Iron–Oxo–Cerium Intermediate in Iron-Catalysed Water Oxidation. *Nat. Commun.* **2015**, *6*, 5865.

(57) Bucci, A.; Savini, A.; Rocchigiani, L.; Zuccaccia, C.; Rizzato, S.; Albinati, A.; Llobet, A.; Macchioni, A. Organometallic Iridium Catalysts Based on Pyridinecarboxylate Ligands for the Oxidative Splitting of Water. *Organometallics*, **2012**, *31*, 8071–8074.

(58) Puerta-Oteo, R.; Jiménez, M. V.; Pérez-Torrente, J. J. Molecular water oxidation catalysis by zwitterionic carboxylate bridge-functionalized bis-NHC iridium complexes. *Catal. Sci. Technol.*, **2019**, Advance article, http://dx.doi.org/10.1039/C8CY02306A.

(59) Corbucci, I.; Petronilho, A.; Müller-Bunz, H.; Rocchigiani, L.; Albrecht, M.; Macchioni, A. Substantial Improvement of Pyridine-Carbene Iridium Water Oxidation Catalysts by a Simple Methyl-to-Octyl Substitution. *ACS Catal.* **2015**, *5*, 2714–2718.

(60) Savini, A.; Bucci, A.; Bellachioma, G.; Rocchigiani, L.; Zuccaccia, C.; Llobet, A.; Macchioni, A. Mechanistic Aspects of Water Oxidation Catalyzed by Organometallic Iridium Complexes, *Eur. J. Inorg. Chem.* **2014**, 690–697.

(61) Dzik, W.I.; Calvo, S.E.; Reek, J. N. H.; Lutz, M.; Ciriano, M. A.; Tejel, C.; Hetterscheid, D. G. H.; De Bruin, B. Binuclear [(cod)(Cl)Ir(bpi)Ir(cod)]$^+$ for Catalytic Water Oxidation. *Organometallics* **2011**, *30*, 372–374.

(62) Savini, A.; Bucci, A.; Nocchetti, M.; Vivani, R.; Idriss, H.; Macchioni, A. Activity and Recyclability of an Iridium-EDTA Water Oxidation Catalyst Immobilized onto Rutile TiO$_2$. *ACS Catal.* **2015**, *5*, 264–271.

(63) Wang, C.; Wang, J. -L.; Lin, W. Elucidating Molecular Iridium Water Oxidation Catalysts Using Metal-Organic Frameworks: A Comprehensive Structural, Catalytic, Spectroscopic, and Kinetic Study. *J. Am. Chem. Soc.* **2012**, *134*, 19895–19908.

(64) Sanchez Casalongue, H. G.; Ng, M. L.; Kaya, S.; Friebel, D.; Ogasawara, H.; Nilsson, A. In Situ Observation of Surface Species on Iridium Oxide Nanoparticles during the Oxygen Evolution Reaction. *Angew. Chem. Int. Ed.* **2014**, *53*, 7169–7172.

(65) Venturini, A.; Barbieri, A.; Reek, J. N. H.; Hetterscheid, D. G. H. Catalytic Water Splitting with an Iridium Carbene Complex: A Theoretical Study. *Chem. –Eur. J.*, **2014**, *20*, 5358–5368

(66) Usón, R.; Oro, L. A.; Cabeza, J. A. Dinuclear Methoxy, Cyclooctadiene, and Barrelene Complexes of Rhodium(I) and Iridium(I). *Inorg. Synth.* **1985**, *23*, 126-130.

(67) Ulmer, L.; Mattay, J.; Torres-García, H. G.; Luftmann, H. The Use of 2-[(2E)-3-(4-Tert-Butylphenyl)-2-Methylprop-2-Enylidene]Malononitrile as a Matrix for Matrix-Assisted Laser Desorption/Ionization Mass Spectrometry. *Eur. J. Mass Spectrom.* **2000**, *6*, 49–52.

(68) Sherwood, P. M. A. In *Practical Surface Analysis in Auger and X-ray Photoelectron Spectroscopy*; Briggs, D.; Seah, M. P. Eds.; Wiley: New York, 1990, 2nd ed., vol. 1, pp. 657.

(69) Elgrabli, D.; Floriani, M.; Abella-Gallar, S.; Meunier, L.; Gamez, C.; Delalain, P.; Rogerieux, F.; Boczkowski, J.; Lacroix, G. Biodistribution and Clearance of Instilled Carbon Nanotubes in Rat Lung. *Part. Fibre. Toxicol.* **2008**, *5*, 20–33.

(70) Zhou, X.; Zhang, T.; Abney, C.W.; Li, Z.; Lin, W. Graphene-immobilized Monomeric Bipyridine-M^{x+} (M^{x+} = Fe^{3+}, Co^{2+}, Ni^{2+}, or Cu^{2+}) Complexes for Electrocatalytic Water Oxidation. *ACS Appl Mater Interfaces.* **2014**, *12*, 18475–18479.

(71) Simonelli, L.; Marini, C.; Olszewski, W.; Avila, M.; Ramanan, N.; Guilera, G.; Cuartero, V.; Klementiev, K. CLÆSS: The Hard X-ray Absorption Beamline of the ALBA CELLS Synchrotron. *Cogent Physics* **2016**, *3*, 1231987.

(72) Rehr, J. J.; Albers, R. C. Theoretical Approaches to X-ray Absorption Fine Structure. *Rev. Mod. Phys.* **2000**, 72, 621−654.

(73) Rehr, J. J.; Albers, R. C. Theoretical Approaches to X-ray Absorption Fine Structure. *Rev. Mod. Phys.* **2000**, 72, 621−654.

Table of Contents/Abstract Graphic